P2.3 Validation and Improvements of Daytime CRTM Performance Using AVHRR IR 3.7 μm Band

XingMing Liang[1,2*], Alexander Ignatov[1], Yong Han[1], and Hao Zhang[3]

[1]NOAA/NESDIS, Center for Satellite Application and Research (STAR), Camp Springs, MD 20746
[2]CSU, Cooperative Institute for Research in the Atmospheres (CIRA), Fort Collins, CO 80523
[3]CUG, Research Center for Space Science and Technology, Wuhan 430074, China

Abstract

Clear-sky brightness temperatures (BT) in AVHRR Ch3B (3.7 μm), Ch4 (11 μm), and Ch5 (12 μm) are simulated using the community radiative transfer model (CRTM). Reynolds sea surface temperature (SST) and NCEP/GFS upper air fields are used as input to CRTM. The model minus observation (M-O) biases are continuously monitored using the Monitoring of IR Clear-sky radiances over Oceans for SST (MICROS; www.star.nesdis.noaa.gov/sod/sst/micros/) near-real time online tool. Prior analyses in MICROS have shown that at night, M-O biases are well within their expected ranges. However, during daytime, the M-O bias in Ch3B is unrealistically cold (up to ~-20 K) in sun glint areas and warm elsewhere (up to ~+5 K). Additional analyses have shown that these anomalies are due to the quasi-Lambertian surface reflectance model employed in CRTM version 1.1. A specular model based on Cox-Munk facet distribution was tested and found to dramatically reduce the M-O biases (to ~-2 K in sun glint and ~-1 K elsewhere). Based on these analyses, this model was implemented in CRTM version 2. Remaining overall negative M-O bias is due to using daily-average Reynolds SST (which does not resolve diurnal cycle) at night, and larger and more variable biases in sun glint area may be due to the remaining residual imperfection of the empirical Cox-Munk model. Several possible ways to minimize these biases are explored. Comprehensive testing and fine-tuning of the newly adopted surface reflectance model in CRTM v2 is underway using geostationary sensors data, with conclusive results pending inclusion of aerosol absorption and scattering in CRTM.

[*] *Corresponding author address: XingMing Liang, NOAA/NESDIS/STAR, WWB Rm. 603, 5200 Auth Rd, Camp Springs, MD 20746; e-mail: Xingming.Liang@noaa.gov*

1. Introduction

The community radiative transfer model (CRTM, Han et al., 2006) is a key part of the new Advanced Clear-Sky Processor for Oceans (ACSPO) system developed at NESDIS (Liang et al., 2009). CRTM is used in ACSPO in conjunction with Reynolds sea surface temperature (SST) analysis and the National Centers for Environmental Prediction (NCEP) Global Forecast System (GFS) upper air fields to calculate model clear-sky brightness temperatures (BT) in AVHRR Ch3B (3.7 μm), Ch4 (11 μm), and Ch5 (12 μm) onboard NOAA-16, -17, -18, -19, and MetOp-A. Simulated BTs are used in ACSPO to improve cloud masking and quality control and to explore physical SST inversions, in addition to the current regression retrievals. Consistency between modeled and observed BTs is critically important for these applications.

A near real-time, web-based tool, Monitoring of IR Clear-sky Radiances over Oceans for SST (MICROS; www.star.nesdis.noaa.gov/sod/sst/micros/), was set up to monitor global model (CRTM) minus observation (AVHRR), or M-O biases (Liang and Ignatov, 2010). The initial objective of MICROS was validation of clear-sky radiance products generated by ACSPO, through their comparisons with CRTM simulation. Later, MICROS also proved instrumental for validation and improvements of CRTM, and for monitoring AVHRR radiances for stability and cross-platform consistency for the Global Space-based Inter-Calibration System (GSICS) Project.

The initial focus of MICROS analysis was on nighttime data (Liang et al., 2009; Liu et al., 2009; Liang and Ignatov, 2010). Overall, the nighttime M-O biases were found within their expected ranges, uniformly distributed in the retrieval space, and consistent across different AVHRR sensors and platforms. These analyses have lent themselves to in-depth understanding and improvements of some CRTM elements, such as treatment of the out-of-band effect in the spectral response of the NOAA-16 Ch3B, surface emissivity, and parameterization of the transmittance coefficient for wide IR bands.

This paper extends these prior analyses by including daytime data, which are also available in MICROS. Our primary focus here is on AVHRR Ch3B centered at 3.7μm. This band is more transparent than the other two AVHRR IR bands, Ch4 and Ch5, centered at 11 and 12 μm, and critically important for cloud masking and SST retrievals (Petrenko et al., 2010). However, on the solar side of the orbit, Ch3B is strongly affected by the solar radiation reflected by the surface and scattered in the atmosphere. Modeling solar reflectance and scattering in the mid-IR band and its validation is a challenging task and results are limited (Merchant et al., 2008). Both effects are modeled in CRTM v1.1, but careful validation is needed in the full global domain.

In this paper, the quasi-Lambertian surface reflectance model employed in CRTM v1.1 is first validated using two years of MICROS data. Daytime M-O biases in Ch3B are consistently cold in sun glint areas and warm elsewhere. Further analyses have shown that this model is inaccurate. To attempt to improve these biases, a specular surface reflectance model, used in conjunction with Cox-Munk (1954) facet slope distribution and widely accepted in the remote sensing community, was tested. It significantly improves the M-O biases and is now adopted in CRTM v2.0. Possible ways to further minimize the M-O biases are also discussed here, concluding with a summary and outline of future plans.

2. Surface reflectance models adopted in CRTM v1.1 and v2

In a transparent AVHRR Ch3B, angular distribution of top-of-atmosphere (TOA) radiance is mainly driven by the surface reflectance, with relatively small contributions from atmospheric absorption (water vapor, aerosol, and minor gases) and scattering (aerosol). This study concentrates on "first-order" effects of surface reflectance. Section 2.1 describes the quasi-Lambertian surface reflectance model adopted in CRTM v1.1. Validation shows that its performance is suboptimal; as such, section 2.2 proceeds with testing the specular Cox-Munk model, which is widely used in the remote sensing community. This new model validates much better against AVHRR TOA radiances.

2.1. Quasi-Lambertian surface reflectance model adopted in CRTM v1.1

CRTM progressed through several versions during MICROS operations, which commenced in July 2008, but the surface reflectance model remained unchanged during all CRTM upgrades through v1.1. In what follows, the term "CRTM v1.1" refers to the quasi-Lambertian surface model, which defines the surface reflectance and downwelling radiance in a specific way.

Its reflectance is defined as one minus Wu-Smith (1997) emissivity, which, in turn, is defined as an integral overall wave facet's Cox-Munk probability density function (PDF) as follows:

$$\gamma(\theta) = 1 - \bar{\varepsilon}(\theta) \tag{1}$$

$$\bar{\varepsilon}(\theta) = \int_{-\infty}^{\infty}\int_{-\infty}^{\infty} \varepsilon(\chi)\cos(\chi) * \cos(\theta_n)^{-1} P(Zx, Zy)\, dz_x\, dz_y \tag{2}$$

The wave facet reflection geometry used in Equations (1) and (2) is shown in Fig. 1.

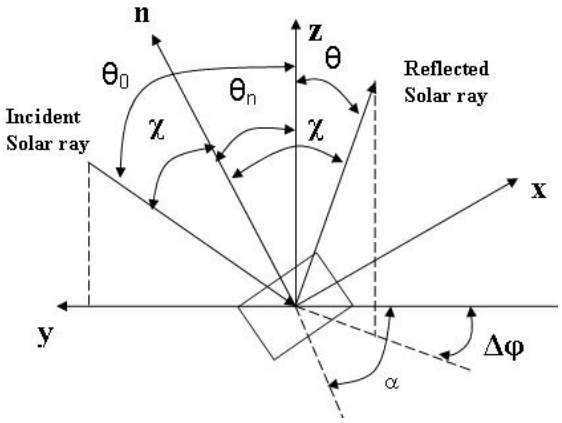

Fig. 1. Geometry of solar reflectance at a wave facet. The +y axis points toward the sun; Z is the local zenith; *n* is the facet unit normal vector, with zenith angle θ_n, and azimuth angle α, respectively.

In Equations (1) and (2), $\gamma(\theta)$ is surface reflectance; $\bar{\varepsilon}(\theta)$ the average Wu-Smith emissivity; θ the view zenith angle; θ_0 the solar zenith angle; $\Delta\varphi$ the relative azimuth angle between the sensor and sun; $\varepsilon(n, \chi)$ the emissivity of the wave facet with the normal vector, *n*; θ_n and α the zenith and azimuth angles of *n*, respectively; and χ the solar incident angle with respect to the wave facet normal, defined as the angle between solar incident direction and *n*. From Fig. 1, the χ and the facet direction can be obtained from the solar incidence and sensor observation directions as

$$\cos(2\chi) = \cos(\theta)\cos(\theta_0) - \sin(\theta)\sin(\theta_0)\cos(\Delta\varphi) \tag{3}$$

$$\cos(\theta_n) = \frac{\cos(\theta) + \cos(\theta_0)}{2\cos(\chi)} \tag{4}$$

$\varepsilon(\chi)$ is the facet emissivity defined as

$$\varepsilon(\chi) = 1 - \rho(\chi) \quad (5)$$

Here, $\rho(\chi)$ is Fresnel reflectivity with respect to the incident angle, χ (e.g., Wu and Smith, 1997). *Zx* and *Zy* are the two slope components of the facet, and *P(Zx,Zy)* is isotropic facet PDF

$$P(Zx, Zy) = P(\theta_n) = \frac{1}{\pi\sigma^2}\exp(-\frac{\tan^2\theta_n}{\sigma^2}) \quad (6)$$

with the mean square slope, σ

$$\sigma^2 = 0.003 + 0.00512w \quad (7)$$

This facet-integrated Wu-Smith emissivity model has been extensively used in remote sensing applications related to the surface emission and reflection of downwelling atmospheric emission (e.g., Hanafin and Minnett, 2005; Seemann et al., 2008). In CRTM v1.1, the co-emissivity is further multiplied by the atmospheric downwelling radiance, specified at a 53º local zenith angle.

This ocean reflectance model is inconsistent with the customary specular model employed to describe the reflected solar radiation, which is described in section 2.2 below. However, it was adopted in CRTM v1.1 for consistency with the land reflectance model, which is known to be closer to Lambertian than to specular, even in the solar part of the spectrum (Han et al., 2006).

Figure 2 shows an example global distribution of the M-O bias for one day of NOAA-18 data on 13 December 2008. The M-O bias is strongly negative in sun glint area and positive elsewhere. For more quantitative analysis, the right panel of Fig. 2 plots the M-O bias as a function of the sun glint angle,

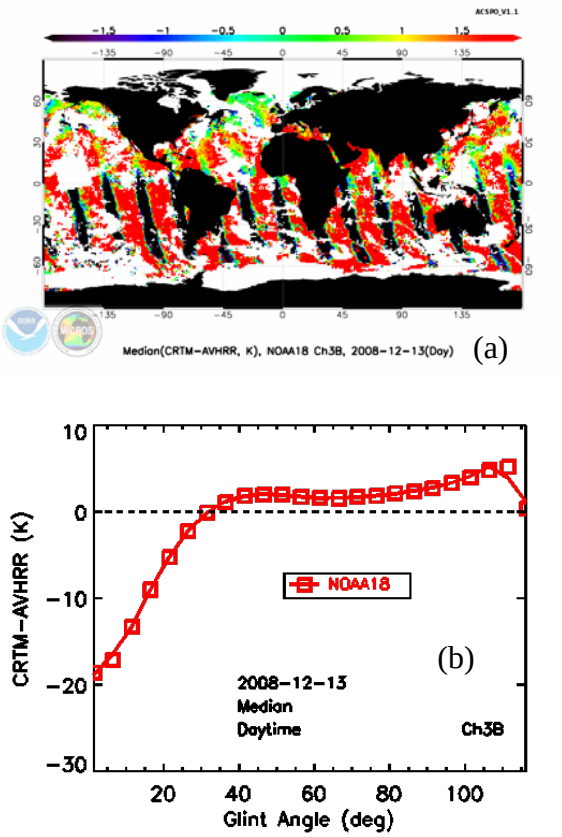

Fig. 2. (a) Global M-O distribution and (b) sun glint angle dependence for NOAA18 Ch3B on 13 December 2008 for CRTM v1.1.

defined as an angle between sensor view and solar specular reflected direction as

$$\cos(\theta_g) = \cos(\theta)\cos(\theta_0) + \sin(\theta)\sin(\theta_0)\cos(\Delta\varphi) \quad (8)$$

A Hovmöller diagram is additionally shown in Fig. 3. It confirms that the large cold bias up to ~-20 K in sun glint area, and a warm bias up to ~+5 K elsewhere, have been persistent during the full two-year period analyzed in MICROS.

We thus conclude that the quasi-Lambertian surface reflectance model employed in CRTM v1.1 is inadequate for ocean applications and improved formulation is needed. This formulation is described in section 2.2 below.

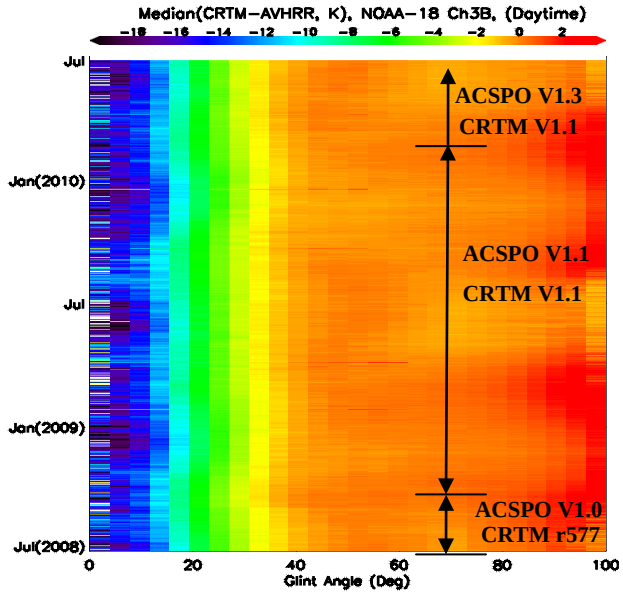

Fig. 3. Hovmöller plot of daytime M-O bias in NOAA-18 Ch3B from July 2008 to July 2010. Glint angle is binned at 4°.

2.2. Specular surface reflectance model employed in CRTM v2

Ocean surface is a specular reflector, as opposed to land which is a near-Lambertian reflector. A specular model used in conjunction with the Cox and Munk (1954) PDF has been extensively used in a wide range of ocean remote sensing applications (e.g., Cox and Munk, 1956; Breon, 1993; Gordon, 1997; Breon and Henriot, 2006; Watts et al., 1996). In this model, the solar reflectance is calculated as

$$\gamma(\theta) = \frac{\pi\rho(\chi)}{4\cos(\theta_0)\cos(\theta)\cos^4(\theta_n)} P(Zx, Zy) \quad (9)$$

Also, the downwelling radiance is specified at a specular direction corresponding to the sensor view zenith angle (rather than at a 53° fixed direction as in CRTM v1.1).

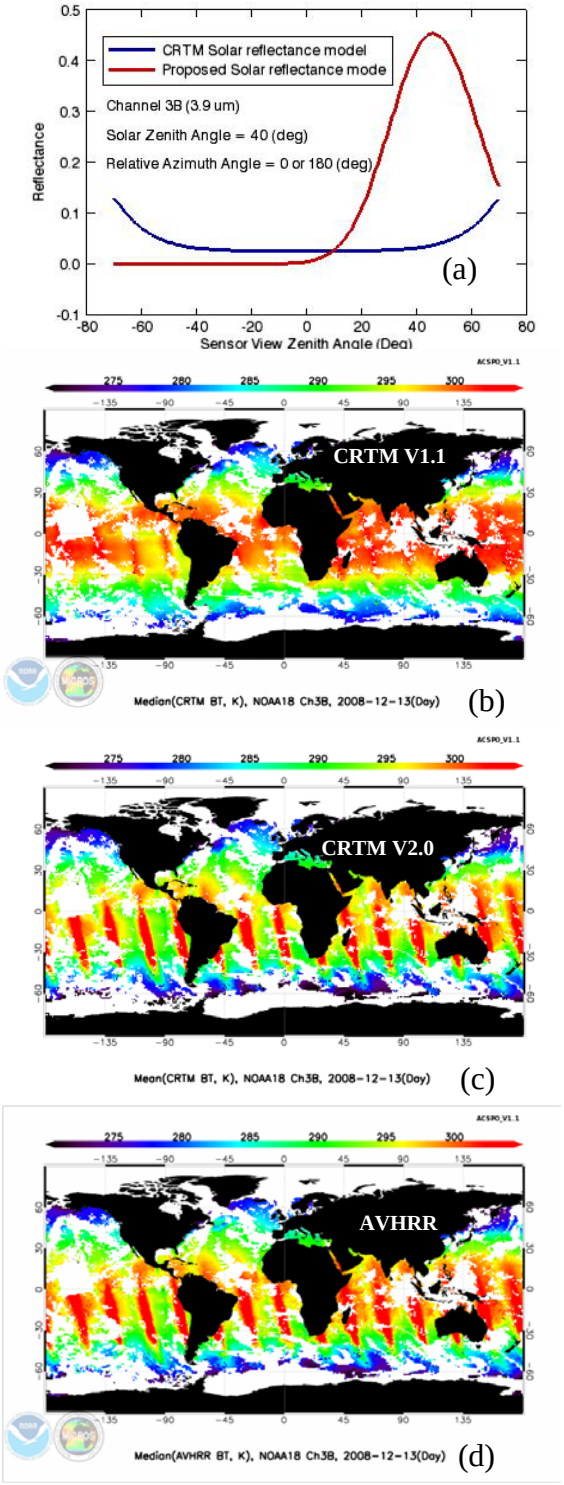

Fig. 4. (a) View zenith angle dependence of surface reflectances employed in CRTM v1.1 and v2 in the principal plane (solar zenith angle = 40°). BTs in NOAA-18 Ch3B on 13 December 2008: (b) CRTM v1.1; (c) CRTM v2; and (d) AVHRR measured.

Figure 4(a) shows an example of the view zenith angle dependence of the two surface reflectances employed in CRTM v1.1 and v2 in the principal plane (solar zenith angle = 40º, relative azimuth angle = 0º on the solar side and = 180º on the anti-solar side; wind speed is fixed at 5 m/s). The strongest sun glint signal is expected at the glint angle = 0º, i.e., on the solar side (relative azimuth angle = 0º) and at a view zenith angle = 40º. The surface reflectance model adopted in CRTM v2 does peak at that point and then reduces steeply as glint angle departs from 0°, reaching ~0 at glint angle ~40º, which approximately corresponds to the edge of the sun glint area. For the quasi-Lambertian surface, on the other hand, surface reflectance is fairly flat at ~0.04, but increases towards the sensor scan edge. Compared to specular reflectance, quasi-Lambertian reflectance is thus underestimated in sun glint area and overestimated elsewhere. This is largely consistent with patterns seen in Figures 2 and 3. Figure 4(c) shows that the new surface reflectance model used in CRTM v2 is not only based on solid physical consideration, but it also very closely reproduces the glint patterns observed in AVHRR BTs (Fig. 4d). On the other hand, the BTs simulated with CRTM v1.1 fail to reproduce these patterns (Fig. 4b).

Figure 5 shows that the new model significantly improves the global M-O bias, which is now within ~-1 to -2 K.

Figure 6 (a and b) extends validation shown in Figure 5(b) by showing five NOAA-18 data sets covering different seasons in July, August, October, November, and December 2008. Six-day time windows were used in Fig. 6 (as opposed to the one-day average shown in Fig. 5), to ensure representativeness of the corresponding data sets. All glint angle dependencies in Fig. 6 (a and b) closely reproduce those seen in Fig. 5(b).

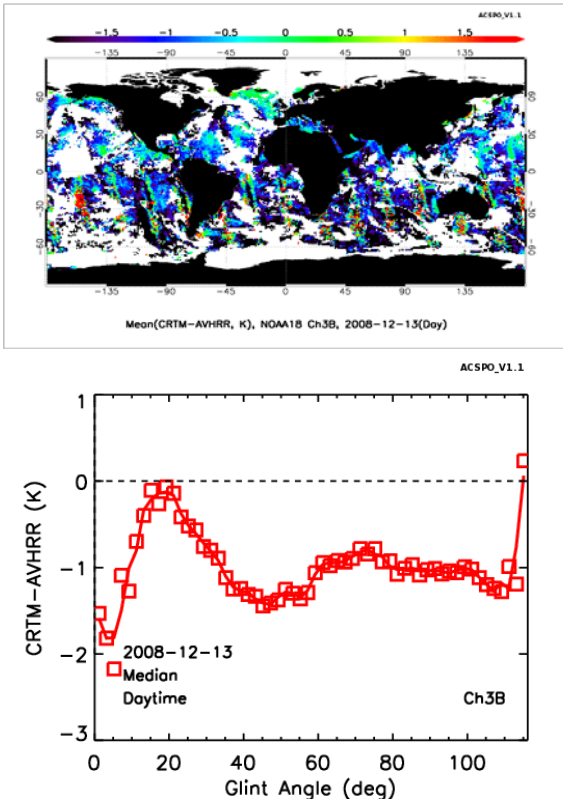

Fig. 5. Same as Fig. 2 but using CRTM v2.

Fig. 6 (c and d) additionally show wind speed dependencies of the M-O bias. Most of the M-O biases are negative during daytime, both in the glint area and outside. This is expected because CRTM uses daily average Reynolds SST (i.e., with diurnal cycle unresolved) as input. As a result, model BTs are underestimated during daytime, when the input SST is colder than actual, due to the effect of diurnal warming. The M-O biases are largest at low winds, when diurnal warming is largest, and decrease with wind speed (Gentemann et al., 2003, 2009). All five curves show nearly the same shape.

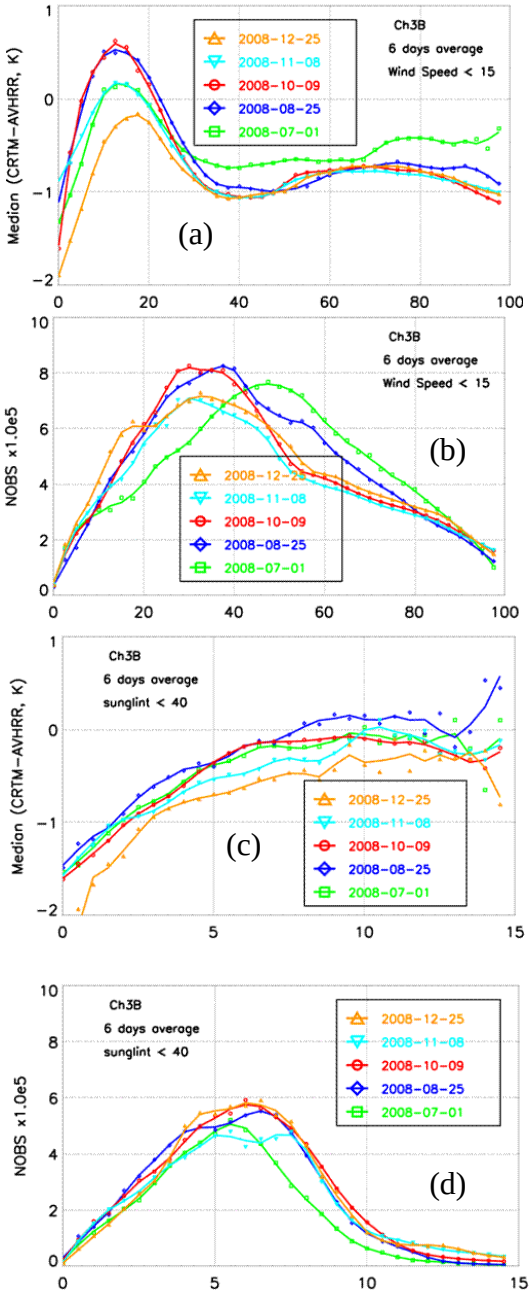

Fig. 6. (a) Glint angle and (c) wind speed dependencies of M-O biases in NOAA-18 Ch3B using CRTM v2, and (b) and (d) corresponding histograms. To minimize the effect of outliers, data with wind speeds of >15 m/s were removed when found to have glint angle dependencies. In case of wind speed dependencies, glint angle was limited to <40° to focus on sun glint area. Each curve represents cumulative statistics over a 6-day period, with the first day of the 6-day period shown (for instance, the 2008-12-25 curve is cumulative over a period from 25 to 30 December 2008).

Non-flat structure in the sun glint area (θg<40°) may be due to remaining inaccuracies in the CM empirical model.

This new specular model was thus adopted in CRTM v2. Overall, it shows dramatic improvement in the daytime M-O bias in Ch3B, compared to the quasi-Lambertian model used in CRTM v1.1. At the same time, the remaining M-O bias may reach 1 to 2 K, is non-uniform in space, and shows complex structure as a function of glint angle and wind speed. It should be minimized and made more uniform across the retrieval space, before CRTM data can be used for accurate cloud screening and SST retrievals during daytime. Improvement options are discussed in the next section.

3. Improvement options

3.1. PDF alternatives to Cox-Munk model

The Cox-Munk empirical PDF (CM) was obtained in 1953 based on 29 photographs taken over a period of 20 days in one geographic area. The derived CM model, however, proved remarkably robust and has been widely used for many ocean remote sensing applications (Masuda et al., 1988; Gordon, 1997; Wu and Smith, 1997).

Some recent studies attempted to improve the CM model, using larger volumes of satellite data over global oceans. In particular, Ebuchi and Kizu (2002) (hereafter, EK) used about 30 million data points from the Visible and Infrared Spin Scan Radiometer (VISSR) onboard Geostationary Meteorological Satellite (GMS-5) over a four-year period and corresponding wind data from NASA Scatterometer (NSCAT) from the Advanced Earth Observation Satellite (ADEOS). No atmospheric correction was applied to VISSR

data; therefore, the derived model is actually the TOA model. They found a significant difference from the CM model; namely, their facets' distribution was narrower than the CM model and its wind direction dependence was weaker:

$$\sigma^2 = 0.0101 + 0.00219w \qquad (10)$$

Another representative study was done by Breon and Henriot (2006) (hereafter, BH). They took 9 million data from the POLarization and Directionality of the Earth Reflectances (POLDER) together with wind data from NSCAT, both onboard ADEOS-1. Atmospheric and foam correction was performed using retrievals in off-glint areas. Their inverted PDF was also slightly different from the CM model:

$$\sigma^2 = 0.004 + 0.00501w \qquad (11)$$

Figure 7 shows histograms of the M-O biases and glint angle dependencies for the CM, BH, and EK models. The M-O bias and standard deviation for the EK model are significantly larger, and its glint angle dependence in the glint area (θg<40°) shows a very different behavior from the other two models. Based on their analyses of MODIS data, Zhang and Wang (2010) independently confirmed that the EK model was outperformed by the CM model. This may be due to the fact that the EK analyses were done in TOA reflectances, and their cloud detection was admittedly suboptimal. On the other hand, the performance of the CM and BH models is comparable (cf. Zhang and Wang, 2010). Note that the BH is a relatively new model and needs further validation (Munk, 2009). Thus, the CM model appears an optimal selection for CRTM v2.

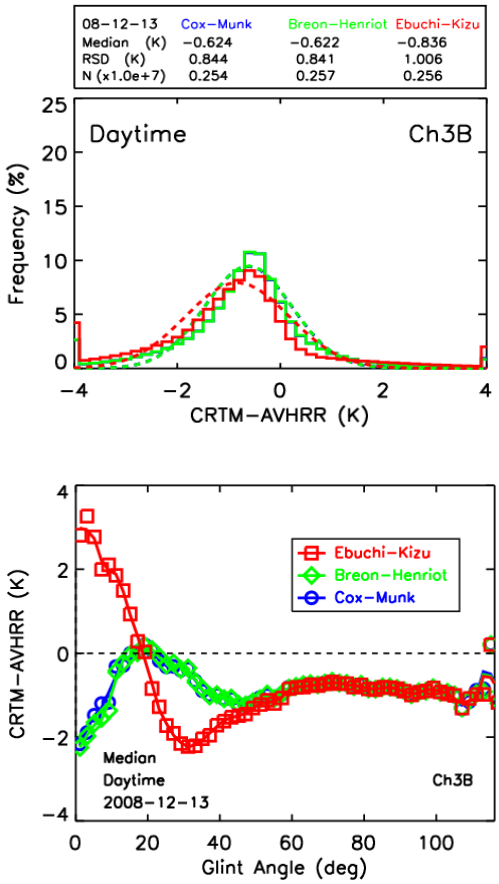

Fig. 7. The global histogram and glint angle dependences for the CM, BH, and EK PDF models using CRTM v2.

3.2. Estimating PDF from AVHRR data

The PDF which is most consistent with the AVHRR data analyzed in this study should be derived from this data itself. In this section, an empirical PDF is estimated by inverting the CRTM using daytime radiative transfer equation (RTE), which takes the following form:

$$\overline{R}(\theta) = \varepsilon(\theta)\overline{B}(T_s)\overline{\tau}(\theta) + \overline{L}^{\uparrow}(\theta) + (1-\varepsilon(\theta))\overline{L}^{\downarrow}(\theta)\overline{\tau}(\theta) + RR(\theta) \qquad (12)$$

Note that Equation (12) is written using the correct CRTM v2 formulation, i.e., directional surface reflectance and angle-specific downwelling radiance. Here, the first three terms on the right-hand side of Eq. (12) are surface emission, upwelling atmospheric emission, and reflected downwelling atmospheric emission, respectively (cf. Eq. (1) in Liang et al., 2009).

The last term is the solar reflected radiance, $RR(\theta)$, which can be represented as follows:

$$RR(\theta) = \frac{F}{\pi}\bar{\tau}^{'}(\theta_0)\bar{\tau}(\theta)\gamma(\theta) \qquad (13)$$

Here, F is solar irradiance at the TOA and $\bar{\tau}^{'}(\theta_0)$ and $\bar{\tau}^{'}(\theta)$ are atmospheric transmittances along the solar and view paths. From Equations (9), (12), and (13), the inverted PDF is obtained as:

$$\begin{aligned} P(\theta_n, w) = & (\bar{R}(\theta) - \varepsilon(\theta)\bar{B}(T_s)\bar{\tau}(\theta) \\ & - \bar{L}^{\uparrow}(\theta) - (1-\varepsilon(\theta))\bar{L}^{\downarrow}(\theta)\bar{\tau}(\theta)) \\ & \times 4\cos(\theta_s)\cos(\theta_r)\cos^4(\theta_n) \\ & / F\bar{\tau}^{'}(\theta_0)\bar{\tau}(\theta)\rho(\chi) \end{aligned} \qquad (14)$$

Figure 8(a) plots the inverted PDF and compares it with the CM model as a function of the facet slope angle, θ_n, for all wind speeds for the day of 13 December 2008. The inverted PDF matches the CM PDF very closely, but it drops a little slower away from sun glint. The fact that the CM PDF is close to 0 away from glint, whereas the inverted PDF is >0, is consistent with the negative M-O bias observed out of the sun glint area, which is deemed to be due to a combined effect of unresolved diurnal variability in the input SST and missing aerosol in CRTM. The large uncertainty near 0° of facet slope angle is likely due to small population (cf. histogram in Fig. 8(b)), due to geometrical constraints between the sun incidence and sensor observation directions, and possible flagging of bright direct glint as cloud in ACSPO processing.

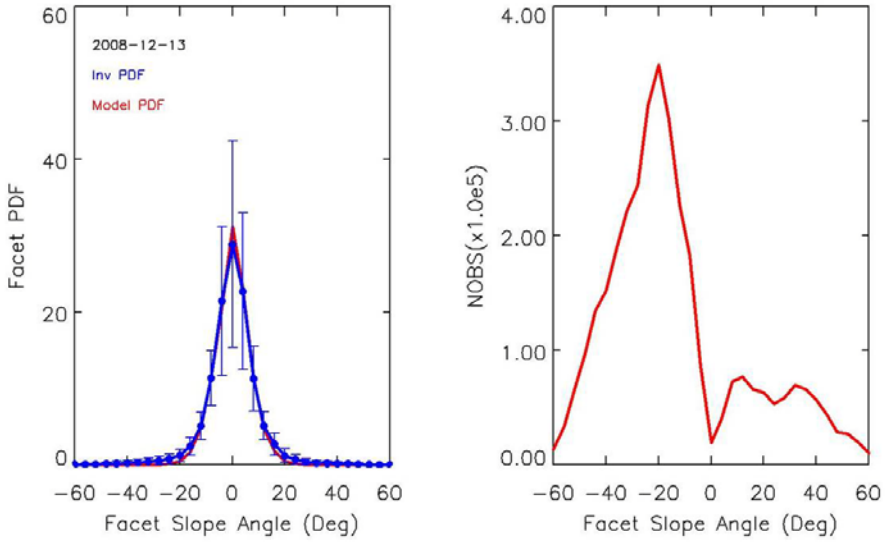

Fig. 8. Inverted and CM PDFs of wave facet slope and corresponding histograms (all wind speeds). Data is the same as in Fig. 2.

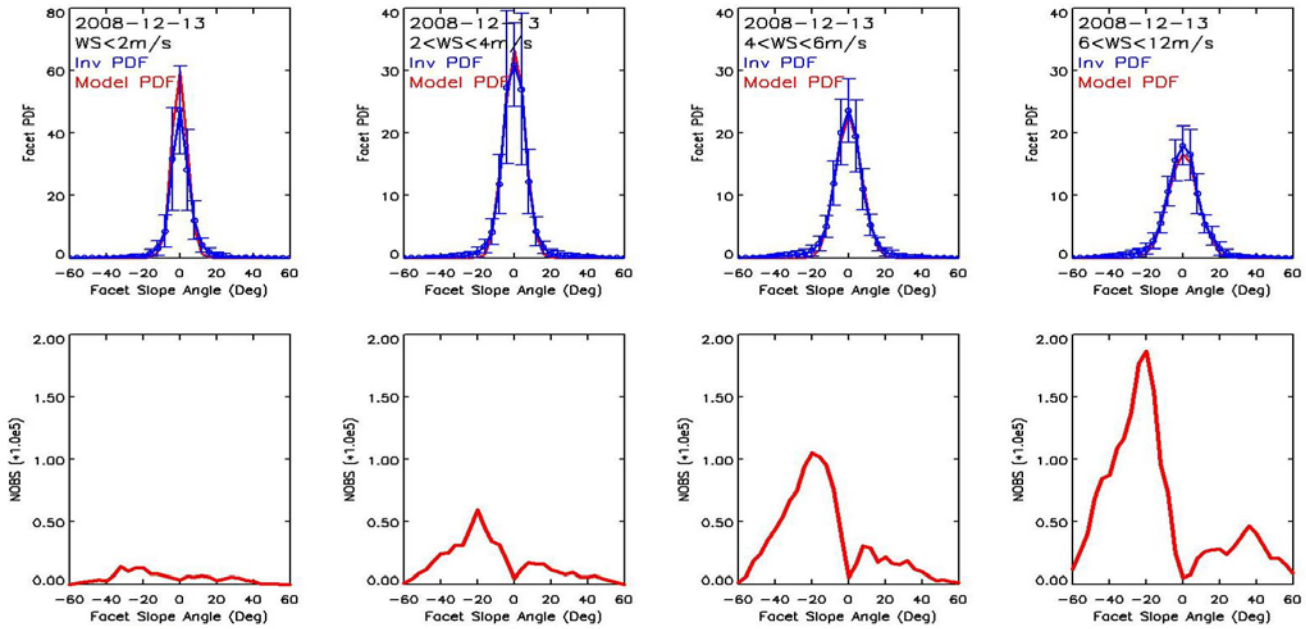

Fig. 9. PDFs of wave facet slope and corresponding histograms stratified by wind speed: (a and b) 0<W<2 m/s; (c and d) 2<W<4 m/s; (e and f) 4<W<6 m/s; and (g and h) 6<W<12 m/s. Data are the same as in Figs. 2 and 8.

To analyze the effect of wind speed on the facet PDF, data were further stratified by wind speed and the result is shown in Figure 9. Overall, the inverted PDF agrees well with the CM model, especially for moderate wind speeds (4<W<6 m/s). However, in the center of the glint area (when facet slope angle is <10°), the CM PDF appears slightly overestimated at low wind speed (W<4 m/s) and underestimated at higher wind speeds (6<W<12 m/s). Due to PDF normalization and negative M-O bias, these relationships are inverted in off-glint areas (when facet slope angle is >10°). These results are preliminary and they will be reexamined when the negative M-O bias is corrected for and aerosol is included in CRTM. This work is currently underway.

4. Conclusion

Based on the statistical analysis in the MICROS web page for two years of data, an unrealistic cold bias (~20 K) in sun glint areas and an unexplained warm bias (~+5 K) in off-glint areas were observed in AVHRR Ch3B during the daytime. This is due to the quasi-Lambertian surface reflectance model employed in the CRTM v1.1. A specular model used in conjunction with Cox-Munk slope distribution, which is based on solid physical consideration and extensively employed in a wide variety of remote sensing applications, was tested. It dramatically improves daytime CTRM BTs and is now adopted in CRTM v2.

The remaining M-O biases in Ch3B reach -1 and -2 K and are unacceptable for highly accurate ACSPO application, including cloud mask and SST inversions. In an attempt to further improve the M-O bias, two other PDFs proposed by Ebuchi and Kizu (2002) and Breon and Henriot (2006) were tested. For the Breon-Henriot model, M-O biases are comparable with the Cox-Munk model, but they are much larger for the Ebuchi-Kizu model. An attempt was subsequently made to

derive the PDF from AVHRR data itself, by inverting the radiative transfer equation. The inverted PDF matches the Cox-Munk model well, except in the immediate vicinity of glint, where a little fine-tuning may be needed at small and large wind speeds. However, these results should be reexamined, after the negative M-O bias is corrected for through resolving diurnal variability in the input SST, and aerosol included in CRTM.

Work is currently underway to explore global aerosol data from the Goddard Chemistry Aerosol Radiation and Transport model (GOCART) as input to CRTM, and re-derive the inverted PDF. Additionally, similar analyses are underway in AVHRR Ch4 and Ch5 to check the sun glint effect on the long-wavelength IR bands. Finally, the proposed model will be comprehensively validated using data from such sources as the Spinning Enhanced Visible and Infrared Imager onboard Meteosat Second Generation geostationary satellites.

Acknowledgement

This work is conducted under the Algorithm Working Group funded by the GOES-R Program Office (Lead, Mitch Goldberg), NPOESS Ocean Cal/Val Program funded by the Integrated Program Office (Lead, Bob Arnone), NOAA Ocean Remote Sensing Program (Manager, Paul DiGiacomo), and Polar PSDI (Manager, Tom Schott). CRTM is provided by NESDIS JCSDA. Thanks go to Mark Liu, Yong Chen, Paul Van Delst, Fuzhong Weng, Yury Kihai, and Nick Nalli for advice and help. The views, opinions, and findings contained in this report are those of the authors and should not be construed as an official NOAA or U.S. Government position, policy, or decision.

References

Breon, F.-M. (1993), An analysis model for the cloud-free atmosphere/ocean system reflectance. *Remote Sens. Environ.*, 43, 179–192.

Breon, F.-M., and N. Henriot (2006), Spaceborne observations of ocean glint reflectance and modeling of wave slope distributions. *J. Geophys. Res.* 111, C06005, doi:06010.01029/02005JC003343.

Cox, C., and W. Munk (1954), Measurements of the roughness of the sea surface from photographs of the sun's glitter. *J. Opt. Soc. Am.*, 44, 838–850.

Cox C., and W. Munk (1956), Slopes of the sea surface deduced from photographs of sun glitter. Bull Scripps Inst Oceanogr Univ Calif, 6, 401–88.

Ebuchi, N., and S. Kizu (2002), Probability distribution of surface wave slope derived using sun glitter images from geostationary meteorological satellite and surface vector winds from scatterometers. *J. Oceanogr.*, 58, 477–486.

Gentemann, C. L., C. J. Donlon, A. Stuart-Menteth, and F. J. Wentz (2003), Diurnal signals in satellite sea surface temperature measurements. *Geophys. Res. Lett.*, 30, doi:10.1029/2002GL016291.

Gentemann, C. L., P. J. Minnett, and B. Ward (2009), Profiles of ocean surface heating (POSH): A new model of upper ocean diurnal warming. *J. Geophys. Res.*, 114, C07017, doi:10.1029/2008JC004825.

Gordon, H. R. (1997), Atmospheric correction of ocean color imagery in the Earth Observing System era. *J. Geophys. Res.* 102, 17081–17106.

Han, Y., P. van Delst, Q. Liu, F. Weng, B. Yan, R. Treadon, and J. Derber (2006), JCSDA Community Radiative Transfer Model (CRTM)–Version 1, NOAA Tech. Rep. NESDIS 122, 33 pp., NOAA, Silver Spring, MD. ftp.emc.ncep.noaa.gov/jcsda/CRTM/CRTM_v1-NOAA_Tech_Report_NESDIS122.pdf

Hanafin, J. A., and P. J. Minnett (2005), Measurements of the infrared emissivity of a wind-roughened sea surface. *Appl. Opt.*, 44, 398–441.

Liang, X., and A. Ignatov (2010), Monitoring of IR Clear-sky Radiances over Oceans for SST (MICROS): near-real time web-based tool for monitoring CRTM – AVHRR biases. *J. Geophys. Res.*, to be submitted. www.star.nesdis.noaa.gov/sod/sst/micros/pdf/micros_JGR.pdf

Liang, X., A. Ignatov, and Y. Kihai (2009), Implementation of the Community Radiative Transfer Model (CRTM) in Advanced Clear-Sky Processor for Oceans (ACSPO) and validation against nighttime AVHRR radiances. *J. Geophys. Res.*, 114, D06112, doi:10.1029/2008JD010960.

Liu, Q, X. Liang, Y. Han, P. van Delst, Y. Chen, A. Ignatov, and F. Weng (2009), Effect of out-of-band response in NOAA-16 AVHRR channel 3B on top-of-atmosphere radiances calculated with the Community Radiative Transfer Model. *J. Atmos. Oceanic Technol.*, doi:10.1175/2009JTECHA1259.1, 2009.

Masuda, K., T. Takashima, and Y. Takayama (1988), Emissivity of pure and sea waters for the model sea surface in the infrared window regions. *Rem. Sens. Env.*, 24, 313–329

Merchant, C. J., A. R., Harris, E. Maturi, O. Embury, S. N, MacCallum, J, Mittaz, and C. P. Old (2008), Sea surface temperature estimation from the Geostationary Operational Environmental Satellite-12 (GOES-12). *J. Atmos. Oceanic Technol.*, 26, 570−581.

Munk, W. (2009), An inconvenient sea truth: spread, steepness, and skewness of surface slopes. *Ann. Rev. Mar. Sci.*, 1, 377–415.

Petrenko, B., A. Ignatov, Y. Kihai, and A. Heidinger (2010), Clear-sky mask for the Advanced Clear-Sky Processor for Oceans. *J. Atmos. Oceanic Technol.*, doi: 10.1175/2010JTECHA1413.1.

Seemann, S. W., E. E. Borbas, R. O. Knuteson, G. R. Stephenson, and H. Huang (2008), Development of a global infrared land surface emissivity database for application to clear-sky sounding retrievals from multispectral satellite radiance measurements. *J. Atmos. Oceanic Technol.*, DOI: 10.1175/2007JAMC1590.1

Watts, P. D., M. R. Allen, and T. J. Nightingale (1996). Wind speed effects on sea surface emission and reflection for the Along Track Scanning Radiometer. *J. Atmos. Oceanic Technol.*, 13, 126–141.

Wu, X., and W. L. Smith (1997), Emissivity of rough sea surface for 8– 13um: Modeling and verification. *Appl. Opt.*, 36, 2609–2618, doi:10.1364/AO.36.002609.

Zhang, H., and M. Wang (2010), Evaluation of sun glint models using MODIS measurements. *J. Quant. Spectrosc. Radiat. Transfer*, 111, 492–506.